ARTICLE

Tuning the Magneto-Transport Properties of Nickel—Cyclopentadienyl Multidecker Clusters by Molecule—Electrode Coupling Manipulation

Zelong Yi,[†] Xin Shen,[†] Lili Sun,[†] Ziyong Shen,[†] Shimin Hou,[†,*] and Stefano Sanvito[‡]

[†]Key Laboratory for the Physics and Chemistry of Nanodevices, Department of Electronics, Peking University, Beijing 100871, People's Republic of China, and [‡]School of Physics and CRANN, Trinity College, Dublin 2, Ireland

ABSTRACT Spin transport in a series of organometallic multidecker clusters made of alternating nickel atoms and cyclopentadienyl (Cp) rings is investigated by using first-principles quantum transport simulations. The magnetic moment of finite Ni_nCp_{n+1} clusters in the gas phase is a periodic function of the number of NiCp monomers, *n*, regardless of the cluster termination and despite the fact that the band structure of the infinite $[NiCp]_\infty$ chain is nonmagnetic. In contrast, when the clusters are sandwiched between gold electrodes, their spin polarization is found to strongly depend on the molecule—electrode coupling. On the one hand, a substantial magnetic moment and a large spin polarization can be detected for $NiCp_2$ and Ni_4Cp_5 with both weak and modest molecule—electrode coupling. On the other hand, when the coupling of the clusters is strong and mediated by Ni adatoms, the spin polarization of all Ni_nCp_{n+1} ($n = 1-4$) clusters is destroyed, although their low-bias conductance is large. This demonstrates that the magnetism and the spin-transport properties of fragile molecular magnets, such as Ni_nCp_{n+1}, can be tuned in a controllable way by changing the contact geometry.

KEYWORDS: multidecker clusters and nanowires · nanomagnetism · spin transport · molecule—electrode coupling · density functional theory · non-equilibrium Green's function

Spintronics is winning growing attention as a technological platform for logic and memory devices as the more conventional silicon-based microelectronics faces serious challenges of the nanometer length scale.[1] In this context, the ability to manipulate electron spins in molecular materials offers a new and extremely tantalizing prospect for spintronics, from both fundamental and technological points of view.[2−4] In particular, the idea of producing all-organic spintronics devices is attractive,[4] where the magnetic properties of the organic material can be manipulated electrically.[5] These future devices will require organic spin injectors, that is, organic magnets with large spin polarization at room temperature. In recent years, many linear molecular clusters with unique spin polarization properties have been proposed theoretically. First-row transition metal multidecker clusters, whose spin polarization is dominated by the 3d electrons of the metal atoms, are a good example.[6−19] Vanadium—benzene (V_nBz_{n+1}) and iron—cyclopentadienyl (Fe_nCp_{n+1}) multideckers are two representative members of such a family. If made in practice, these compounds will have extremely attractive properties. For instance Fe_nCp_{n+1} clusters have been predicted to be the first half-metallic linear molecules with high spin filter efficiency (SFE). Furthermore, two-terminal devices based on Fe_nCp_{n+1} are expected to show negative differential resistance.[16]

Most of the research to date has focused on molecular wires with a robust half-metallic electronic structure in either a bulk (infinite) one-dimensional form[9,10,12,13,16,18] or as finite clusters sandwiched between ferromagnetic electrodes.[20−22] The present work investigates a conceptually different material system, namely, we look at the magnetically fragile Ni_nCp_{n+1} clusters attached to gold electrodes. Although the band structure of the parental infinite $[NiCp]_\infty$ chain is not spin-polarized, finite Ni_nCp_{n+1} clusters do exhibit a spin polarization. Intriguingly, such a spin polarization depends on the details of the specific cluster, with a periodic dependence of the magnetic moment over the number of NiCp monomers in the molecule.

This study is based on a fully self-consistent *ab initio* approach, which combines the non-equilibrium Green's function (NEGF) formalism with spin density functional

*Address correspondence to smhou@pku.edu.cn.

Received for review December 7, 2009 and accepted March 08, 2010.

Published online March 16, 2010. 10.1021/nn901784t

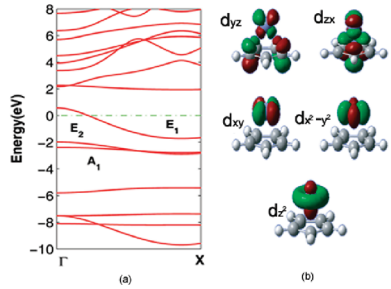

Figure 1. Band structure (a) of the infinite $[NiCp]_\infty$ chain and charge density isosurfaces of the crystalline orbitals (b) corresponding to the Ni 3d shell calculated at the Γ point. The Fermi level is set to zero.

theory (DFT), that is, the NEGF+DFT method.[23−33] Our results show that the spin-transport properties of finite Ni_nCp_{n+1} clusters depend critically on their coupling strength to the electrodes. In particular, when the bonding between the molecule and the electrodes is weak or modest, large charge spin polarization (CSP) and high SFE can be realized for certain Ni_nCp_{n+1} clusters. In contrast, strong molecule−electrode coupling always destroys the spin polarization and turns Ni_nCp_{n+1} into high transmission diamagnetic molecules.

RESULTS AND DISCUSSION

Electronic Structure of the Infinite $[NiCp]_\infty$ Chain and Finite Ni_nCp_{n+1} Clusters. We start our analysis by looking at the electronic structure of the main building blocks of our proposed devices, namely, Ni_nCp_{n+1} clusters in the gas phase. Let us first look at their structural properties. The C−C and C−H bond lengths in the Cp ring for the eclipsed infinite $[NiCp]_\infty$ chain are optimized, respectively, to be 1.461 and 1.096 Å, with the perpendicular distance between the nickel atom and the Cp ring being 1.825 Å. The calculated band structure is shown in Figure 1a. In contrast to the infinite $[FeCp]_\infty$ chain, which has the electronic structure of a half-metal with a magnetic moment per unit cell of 1.0 μ_B,[16−18] $[NiCp]_\infty$ is only a normal metal. Its electronic structure is not spin-polarized, and a doubly degenerate band cuts across the Fermi level (E_F). This indicates that the Hund's energy for Ni is much weaker than that for Fe.

In Figure 1b, we provide additional details of the energy bands around E_F by presenting the crystalline orbitals associated with the Ni 3d levels and calculated at the Γ point. As one can see from the figure, the band located at 0.6 eV is doubly degenerate and composed of both Ni $3d_{xz}$ (or $3d_{yz}$) and Cp ring π-type orbitals, while that at −1.8 eV is also doubly degenerate with the main orbital contributions coming from Ni $3d_{xy}$ (or $3d_{x^2-y^2}$). In contrast, the band at −2.1 eV is not degenerate, and its wave function is mainly composed of Ni $3d_{z^2}$. Similarly to $[FeCp]_\infty$,[17,18] we can rationalize the electronic structure of the infinite $[NiCp]_\infty$ chain in terms of a charge-transfer mechanism as follows. Although an isolated Ni atom has the $[Ar]3d^84s^2$ electronic configuration, in the chain, the Ni s-shell is lifted in energy to above E_F, and the strong D_{5h} crystalline field splits the d-shell into the A_1 (d_{z^2}) singlet and the E_2 (d_{xy}, $3d_{x^2-y^2}$) and E_1 (d_{xz}, d_{yz}) doublets. One of the 10 valence electrons is transferred from Ni to the Cp ring, thus forming a Cp^-/Ni^+ ionic structure. Since six valence electrons completely fill the lower-lying two bands with A_1 and E_2 symmetry, the remaining three valence electrons can only partially occupy the doubly degenerate E_1 band. Consequently, the E_1 band crosses E_F, and the eclipsed infinite $[NiCp]_\infty$ chain remains a normal metal. We have also examined the staggered infinite $[NiCp]_\infty$ chain, where the neighboring Cp rings are rotated by 36° with respect to each other, and find that this has the same electronic structure of the eclipsed one. Given their close similarity and in the spirit of brevity, only the eclipsed configuration is considered in what follows.

We now move our attention to finite Ni_nCp_{n+1} (n = 1−8) clusters. The C−C bond length and the perpendicular Ni−Cp distance for $NiCp_2$ are optimized, respectively, to 1.444 and 1.815 Å, both being slightly smaller than the corresponding values in $[NiCp]_\infty$. In contrast, the C−H bond lengths in the Cp rings are calculated to be 1.096 Å; that is, they are the same in $NiCp_2$ and $[NiCp]_\infty$. When compared to the experimental geometry of $NiCp_2$ in the gas phase,[34] namely, 1.430 Å (C−C), 1.083 Å (C−H), and 1.823 Å (Ni−Cp), both the C−C and C−H bond lengths are slightly overestimated while the Ni−Cp distance is slightly underestimated. In the larger Ni_nCp_{n+1} (n = 2−8) clusters, depending on the precise location within the molecule, the Cp C−C bond

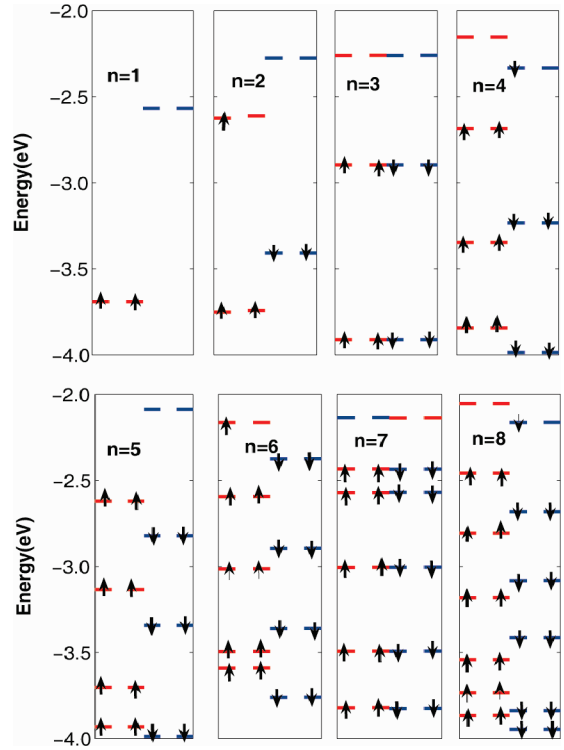

Figure 2. Energy diagram of the frontier molecular orbitals of Ni_nCp_{n+1} (n = 1−8) clusters for spin-up (red) and spin-down (blue) electrons.

TABLE 1. Magnetic Moments (M) of Finite Multidecker Clusters Composed of Ni Atoms and Cp Rings

cluster	M (μ_B)	cluster	M (μ_B)	cluster	M (μ_B)
$NiCp_2$	2	Ni_3Cp_2	2	Ni_2Cp_2	2
Ni_2Cp_3	1	Ni_4Cp_3	1	Ni_3Cp_3	1
Ni_3Cp_4	0	Ni_5Cp_4	0	Ni_4Cp_4	0
Ni_4Cp_5	1	Ni_6Cp_5	1	Ni_5Cp_5	1
Ni_5Cp_6	2	Ni_7Cp_6	2	Ni_6Cp_6	2
Ni_6Cp_7	1	Ni_8Cp_7	1	Ni_7Cp_7	1
Ni_7Cp_8	0	Ni_9Cp_8	0	Ni_8Cp_8	0
Ni_8Cp_9	1	$Ni_{10}Cp_9$	1	Ni_9Cp_9	1

lengths vary in the range of 1.446−1.460 Å and the Ni−Cp distance varies in the range of 1.795−1.844 Å, while the C−H bond lengths remain almost unchanged.

Since the low-bias junction conductance is significantly affected by frontier molecular orbitals, it is interesting to take a look at the energy diagrams of Ni_nCp_{n+1} ($n = 1-8$), which are shown in Figure 2. An important feature of Ni_nCp_{n+1} clusters is that many frontier molecular orbitals are doubly degenerate and their spin state is quite different from that of the parental infinite $[NiCp]_\infty$. The magnetic moments of the various clusters are listed in the second column of Table 1. As we can see, among the eight Ni_nCp_{n+1} clusters investigated here, only Ni_3Cp_4 and Ni_7Cp_8 are a nonmagnetic singlet, with the other six in either a doublet or a triplet ground state. Intriguingly, we notice that Ni_nCp_{n+1} and $Ni_{n+4}Cp_{n+5}$ have the same magnetic moment regardless of n, indicating that the magnetic moment of a finite Ni_nCp_{n+1} cluster is a periodic function of the number of NiCp monomers with a period of four. Furthermore, we have carried out additional calculations for clusters as long as to 16 NiCp monomers (not shown here) and found that the periodicity of the magnetic moment is kept at least up to those lengths. This indicates that the diamagnetic ground state of $[NiCp]_\infty$ can be recovered for substantially longer clusters.

The electronic properties of finite Ni_nCp_{n+1} clusters can also be understood by the charge-transfer mechanism used for the infinite case. For a given Ni_nCp_{n+1} cluster, the Ni atoms provide $10n$ valence electrons in total. Among these, $n + 1$ are captured by the Cp rings to form the more stable Cp^- anions, while $6n$ completely fill the $3n$ molecular orbitals composed of Ni 3d levels of A_1 and E_2 symmetry. The remaining $3n - 1$ valence electrons occupy n doubly degenerate molecular orbitals composed of the Ni 3d levels of E_1 symmetry and the π-type orbitals of the Cp rings. The details of the filling of such extremal orbitals determine the magnetic state of the cluster. Thus for nickelocene, $NiCp_2$, Hund's rule requires the remaining two valence electrons to occupy the doubly degenerate molecular orbital with the same spin orientation, resulting in a triplet state. In contrast for Ni_2Cp_3, four of the five remaining valence electrons completely fill the lower molecular orbital, while the final electron occupies the upper one in a doublet configuration. Then, in Ni_3Cp_4, the eight remaining valence electrons fill completely the two lower doubly degenerate molecular orbitals, resulting in a singlet state. Finally, 8 of the 11 valence electrons of Ni_4Cp_5 fill completely the two lowest molecular orbitals, while the remaining three electrons partially occupy the upper molecular orbital, resulting again in a doublet spin state. When compared with Ni_nCp_{n+1} ($n = 1-4$), the $Ni_{n+4}Cp_{n+5}$ cluster has 12 additional valence electrons and 4 more doubly degenerate molecular orbitals. These 12 valence electrons fill the three lowest molecular orbitals completely, thus that the magnetic moment of the $Ni_{n+4}Cp_{n+5}$ cluster is the same as that of Ni_nCp_{n+1}.

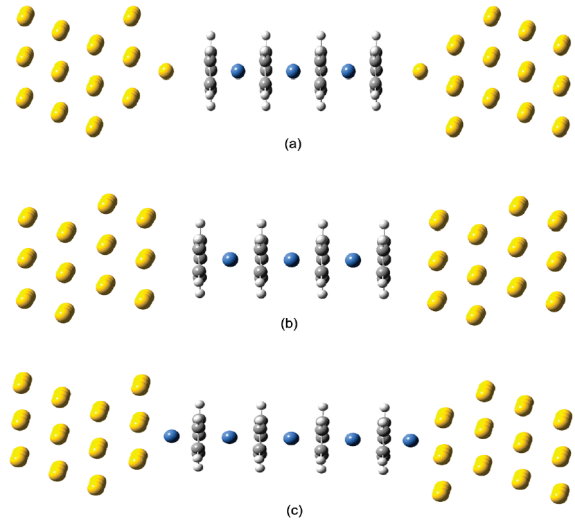

Figure 3. Optimized anchoring structure of a Ni_nCp_{n+1} cluster sandwiched between two gold electrodes. Here the Ni_3Cp_4 cluster is chosen as a representative member of the Ni_nCp_{n+1} family. (a) Two gold adatoms are used as linkers; (b) face-to-face geometry; (c) two nickel adatoms are used as linkers.

Furthermore, we also investigate both $Ni_{n+2}Cp_{n+1}$ and $Ni_{n+1}Cp_{n+1}$ ($n = 1-8$) clusters. These are constructed by adding one more Ni atom either at both or only at one side of the parental Ni_nCp_{n+1} cluster. The calculated magnetic moments are listed in the fourth and sixth columns of Table 1. The most interesting result for these two different classes of clusters is that the spin state of $Ni_{n+2}Cp_{n+1}$ and $Ni_{n+1}Cp_{n+1}$ is identical to that of the corresponding Ni_nCp_{n+1}. In fact, for every Ni atom attached to Ni_nCp_{n+1}, 10 more valence electrons and five more 3d orbitals are added. The 10 valence electrons completely fill the five 3d orbitals, thus the additional Ni atom does not change the spin state of the cluster.

Transport Properties of Finite Ni_nCp_{n+1} Clusters Attached to Au Electrodes. We now investigate the transport properties of finite Ni_nCp_{n+1} ($n = 1-4$) clusters sandwiched between nonmagnetic Au electrodes. As shown in Figure 3, we consider three different classes of molecule−electrode geometries, in which (**I**) Ni_nCp_{n+1} is attached to the electrodes through one Au adatom on each side

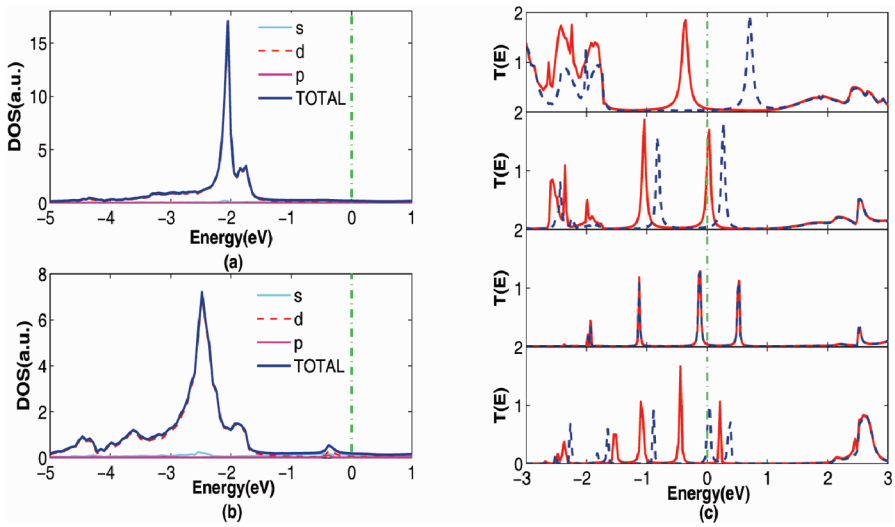

Figure 4. Transport properties of Ni_nCp_{n+1} attached to Au(111) electrodes through two Au adatoms. (a) LDOS of the Au adatom only, and (b) LDOS of the Au adatom when also a Ni_nCp_{n+1} cluster is attached. (c) Energy-dependent spin-resolved transmission spectra of Ni_nCp_{n+1} ($n = 1-4$ when moving from top to bottom): solid red curves for spin-up electrons and dashed blue curves for spin-down.

of the junction (Figure 3a); (**II**) Ni_nCp_{n+1} is attached to the electrodes directly, thus forming a face-to-face contact (Figure 3b); (**III**) Ni_nCp_{n+1} is joined to the electrodes through one Ni adatom on each side. In this last case, the central molecule is essentially a $Ni_{n+2}Cp_{n+1}$ cluster (Figure 3c). A common feature of all these geometries is that either the Au or the Ni adatoms or the outmost Cp rings are placed on top of the Au(111) hollow site, thus the most energetically stable configuration is formed. In order to quantify the spin polarization efficiency of the junction, we use the definition SFE $= (T_{max} - T_{min})/T_{max}$, where T_{max} and T_{min} are, respectively, the maximum and minimum between the transmission coefficients for the spin-up and spin-down channels at E_F. The CSP is defined as CSP $= Q_\uparrow - Q_\downarrow$, where $Q_\uparrow$ and $Q_\downarrow$ are numbers of the spin-up and spin-down electrons, respectively.[10]

The geometry (**I**) is the one displaying the weakest molecule/electrode interaction since the Au adatom is placed at 2.33 Å from the Au(111) surface and 3.02 Å away from the plane of the outmost Cp ring. Since the Cp anions in Ni_nCp_{n+1} capture one additional electron from Ni and a benzene-like stable aromatic configuration is formed, their interaction with the Au adatom is very weak.[35] This is also confirmed by comparing the local density of states (LDOS) of the Au adatom when the Ni_nCp_{n+1} cluster is either in contact to or separated from it. For the separated case (see Figure 4a), the Au 5d orbitals form a sharp peak at about 2.1 eV below E_F, together with a small shoulder at a slightly higher energy. Around E_F, the LDOS is mainly of s-character and rather small. Figure 4b, obtained when the Ni_nCp_{n+1} cluster is in contact with the adatom, reveals a rather similar situation, with the LDOS being only marginally affected by the bonding. We then expect the transport to be dominated by the electronic states of the free-standing Ni_nCp_{n+1} clusters.

The spin-resolved transmission spectra of the Ni_nCp_{n+1} ($n = 1-4$) clusters are shown in Figure 4c. We can observe that all of the clusters retain their spin polarization even after being contacted to the electrodes, with the only exception being that of Ni_3Cp_4, which is nonmagnetic in the gas phase and remains nonmagnetic in the junction. Due to the weak molecule−electrode coupling, only narrow transmission peaks appear around E_F.

In order to gather a deeper understanding into the Ni_nCp_{n+1} conductance, we project the junction transmission onto the frontier molecular orbitals of the central Ni_nCp_{n+1} cluster. This is performed by using our previously developed projection method based on scattering states.[36] For nickelocene, $NiCp_2$, the first transmission peak below E_F corresponds to the spin-up HOMO, while the first transmission peak above E_F originates from the spin-down LUMO. Then, for Ni_2Cp_3, the transmission peak at E_F is contributed by the doubly degenerate spin-up HOMO, while the first transmission peak above E_F corresponds to the doubly degenerate spin-down LUMO. In contrast, the transmission peak at E_F of Ni_4Cp_5 is associated with the doubly degenerate spin-down HOMO, while the first transmission peak above E_F corresponds to the doubly degenerate spin-up LUMO. Thus, there is a spin-polarized resonant transmission at the Fermi level for both Ni_2Cp_3 and Ni_4Cp_5 clusters in geometry **I**. This is dominated by spin-up and spin-down levels, respectively, for Ni_2Cp_3 and Ni_4Cp_5, and in both cases, the spin polarization approaches 100%. For all of the other clusters examined, there are no resonant peaks at the Fermi level, so the transport is tunneling-like and the tail of the

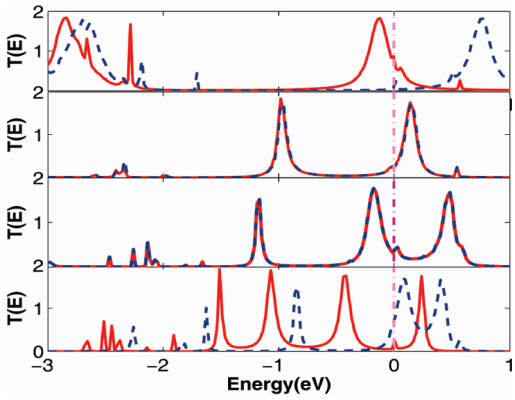

Figure 5. Energy-dependent spin-resolved transmission spectra of Ni_nCp_{n+1} attached to Au(111) electrodes *via* the face-to-face geometry ($n = 1-4$ when moving from top to bottom): solid red curves for spin-up electrons and dashed blue curves for spin-down.

transmission peak closer to E_F determines the spin polarization of the current. Thus, for Ni_3Cp_4, the transmission at E_F is close to zero and it is not spin-polarized, while for $NiCp_2$, the spin polarization is about 53%.

The extraordinary large spin polarization of Ni_2Cp_3 and Ni_4Cp_5 is rather unexpected, considering that the electronic structure of the parental infinite $[NiCp]_\infty$ chain is spin-degenerate. Interestingly, the CSP values for the Ni_nCp_{n+1} clusters attached to gold are 1.88, 0.66, 0.00, and 1.28, respectively, for $n = 1$, 2, 3, and 4. Another interesting fact is that, although in the gas phase Ni_2Cp_3 and Ni_4Cp_5 have the same magnetic moment, they have different CSP values after being contacted to Au electrodes *via* Au adatoms. This originates from the fact that the Ni_2Cp_3 HOMO is occupied by a spin-up electron, while the HOMO of Ni_4Cp_5 is occupied by a spin-down one. All of these transport properties can be rationalized by looking again at the level diagram of Figure 2, where one can note that the HOMOs of Ni_2Cp_3 and Ni_4Cp_5 are singly occupied doubly degenerate orbitals, in contrast to $NiCp_2$ and Ni_3Cp_4, whose HOMOs are fully occupied. This means that, while for the Ni_2Cp_3 and Ni_4Cp_5 clusters the electrodes' Fermi level can pin at the HOMO, it will instead align in the HOMO−LUMO gap for $NiCp_2$ and Ni_3Cp_4.

We now move our attention to geometry **II**. This anchoring structure provides a stronger molecule−electrode coupling than that of **I**, as is demonstrated by the broadening of the peaks in the transmission spectra shown in Figure 5 (the distance between the Au(111) surface and the outmost Cp ring is now 3.39 Å). The transmission of the $NiCp_2$ and Ni_4Cp_5 clusters is still spin-polarized and at the Fermi level is dominated by the spin-up HOMO in $NiCp_2$ and by the spin-down HOMO in Ni_4Cp_5. The resulting spin polarization efficiency is 98.3% for $NiCp_2$ and 65.9% for Ni_4Cp_5; that is, it is reduced from that of **I**. This time Ni_2Cp_3 represents an exception since the enhanced electronic coupling strength to the electrodes destroys its spin polarization. The transmission peak around E_F receives contributions from both the spin-up HOMO and spin-down LUMO, which now merge into a single unpolarized peak centered at 0.11 eV above E_F. Correspondingly, the CSP values of the four Ni_nCp_{n+1} ($n = 1-4$) clusters are 1.47, 0.03, 0.00, and 1.33, respectively, for $n = 1$, 2, 3, and 4.

Finally, the anchoring structure **III** provides the strongest electronic coupling between the molecule and the electrodes among the three geometries examined. The Ni adatoms are now optimized to be 1.98 Å above the Au (111) surface and 1.71 Å from the neighboring Cp ring. In order to obtain a better insight into such a strong interaction, we investigate the LDOS of the Ni adatoms deposited on the Au surfaces in the situations where they are either separated from (Figure 6a) or in contact with the Ni_nCp_{n+1} molecules (Figure 6b); that is, we perform a similar analysis to that done for the Au adatoms in **I**. In the case of Ni, one sharp peak in the LDOS rises at about 0.3 eV below E_F. This is almost completely dominated by Ni 3d atomic orbitals and provides the largest contribution to the LDOS around E_F. When the Ni_nCp_{n+1} cluster is attached to the adatom, the overall shape of the LDOS changes significantly and four sharp peaks appear in the energy range [−2.0 eV, −0.5 eV], demonstrating a strong molecule−electrode electronic coupling.

The corresponding spin-resolved transmission spectra for the Ni_nCp_{n+1} ($n = 1-4$) clusters are shown in Figure 6c. The most striking feature is that the spin polarization of $NiCp_2$, Ni_2Cp_3, and Ni_4Cp_5 clusters is destroyed by the strong molecule−electrode coupling, thus their CSP and SFE both approach zero, despite the fact that the isolated Ni_nCp_{n+1} and $Ni_{n+2}Cp_{n+1}$ ($n = 1$, 2, and 4) clusters are all spin-polarized (see Table 1). Certainly, this strong coupling does enhance the transmission of all four Ni_nCp_{n+1} clusters, and a broad transmission plateau close to $T = 2$ appears around E_F, indicating that several frontier molecular orbitals contribute to the transmission at the Fermi level.

Because of this large molecular orbital mixing, projecting the transmission coefficient onto molecular orbitals is no longer informative. We then employ for further analysis the concept of transmission eigenchannels.[37,38] For all of the four Ni_nCp_{n+1} clusters examined, we find two spin-degenerate eigenchannels contributing equally to the transmission at E_F. The isosurface plots of such eigenchannels for the junction incorporating $NiCp_2$ are displayed in Figure 7a,b. As we can see, in the region of the molecule, the eigenchannels consist of both Ni $3d_{xz}$ or $3d_{yz}$ and Cp π-orbitals. These latter couple strongly to the conducting states of the Au electrodes through the $3d_{xz}$ or $3d_{yz}$ orbitals of the Ni adatoms. Such a conducting behavior can be traced back directly to the electronic structure of the infinite $[NiCp]_\infty$ chain, in which the doubly degenerate E_1

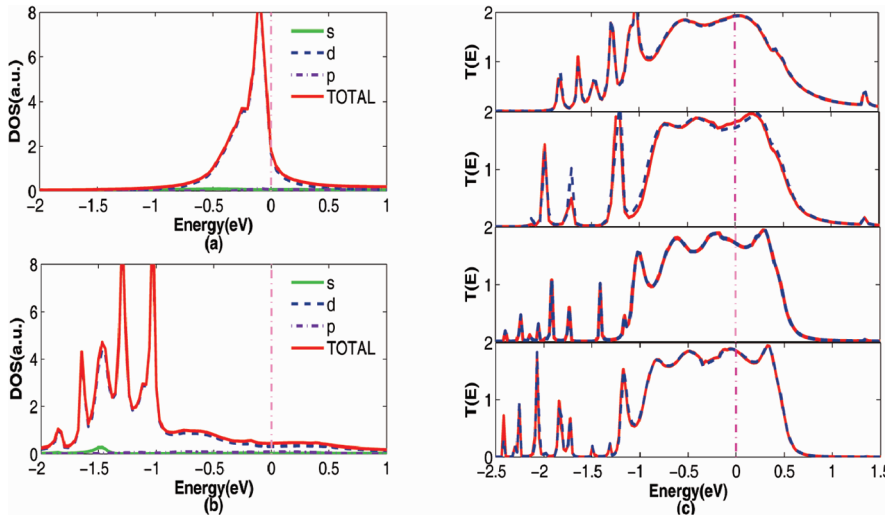

Figure 6. Transport properties of Ni_nCp_{n+1} clusters attached to Au(111) electrodes through Ni adatoms. (a) LDOS of the Ni adatom where there is no molecule, and (b) LDOS of the Ni adatom when the Ni_nCp_{n+1} molecule is attached. (c) Energy-dependent spin-resolved transmission spectra of Ni_nCp_{n+1} ($n = 1-4$ when moving from top to bottom): solid red curves for spin-up electrons and dashed blue curves for spin-down.

band for both spin-up and spin-down electrons cuts across E_F (see Figure 1a). Such a doubly degenerate E_1 band extends into the Au electrodes by coupling with the Ni adatom $3d_{xz}$ or $3d_{yz}$ orbitals and thus provides two highly conducting channels.

In order to obtain a deeper understanding into the role of the Ni adatoms on the transport of the Ni_nCp_{n+1} clusters, we take $NiCp_2$ as a prototye and examine one additional anchoring structure. This is similar to the geometry **III**, but now there is only one Ni adatom at one of the two sides of the molecule, while at the other side, a Cp ring bonds directly to the Au surface. This is named geometry **i**. Its spin-resolved transmission spectrum is shown in Figure 8a. Although spin polarization is now present, the spin filter efficiency is decreased from 98.3% for **II** to only 30.8%. This is due to the enhanced transmission at E_F of the spin-down electrons, indicating that the electrode−molecule coupling strength in **i** is between those of **II** and **III**. The projected transmission analysis shows that for the spin-up electrons the narrow transmission peak centered at −1.0 eV mainly originates from the HOMO, which also largely contributes to the shoulder around E_F. At the same time, the HOMO-2 also makes a small contribution to this peak and to its shoulder. In contrast, the HOMO-1 state does not contribute to the transmission around the Fermi level, only leading to a small peak at about −2.1 eV. When looking at the spin-down transmission, we note that, although the LUMO dominates the transmission at E_F and the first transmission peak above the Fermi level, the transmission peak centered at −0.8 eV receives considerable contributions from the LUMO, HOMO, HOMO-2, and HOMO-3. Again, the HOMO-1 plays a negligible role in the transmission around the Fermi level but dominates the transmission peak at about −2.0 eV.

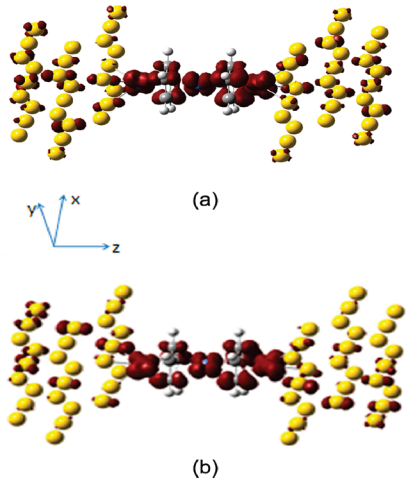

Figure 7. Isosurface plots of the two conducting eigenchannels at the Fermi level for a $NiCp_2$ molecule coupled to two gold electrodes through two Ni adatoms.

When comparing the transport properties of Ni_nCp_{n+1} ($n = 1-4$) clusters contacted to two gold electrodes with different anchoring geometries, we find that $NiCp_2$ and Ni_4Cp_5 exhibit large spin polarization for both weak (**I**) and modest (**II**) electrode−molecule couplings. In contrast, the strong coupling in **III** destroys almost completely the spin polarization of all four Ni_nCp_{n+1} clusters, although their transmission at the Fermi level is much improved. Our results for nickelocene $NiCp_2$ are summarized in Table 2, and one can note that they differ significantly from our previous findings for Fe_nCp_{n+1}.[18] In fact, Fe_nCp_{n+1} ($n > 2$) clusters attached to Pt electrodes through Pt adatoms not only can act as nearly perfect spin filters but also show a large transmission around the Fermi level, as a result of the strong molecule−electrode coupling and the large contribution of d-electrons to the Pt DOS around the Fermi level. These markedly different transport properties between Ni_nCp_{n+1} and Fe_nCp_{n+1} for strong

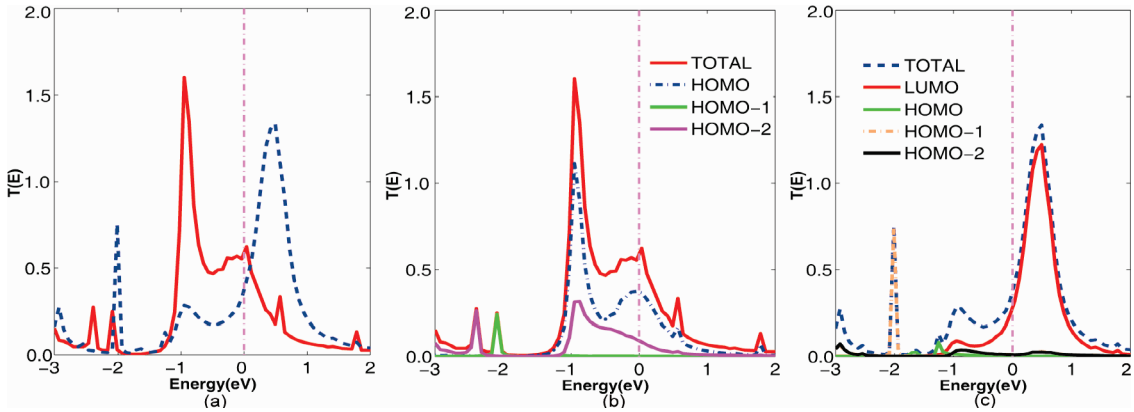

Figure 8. Transport properties of $NiCp_2$ attached to Au(111) electrodes *via* the face-to-face geometry on one side and one nickel adatom on the other. (a) Energy-dependent spin-resolved transmission spectrum: solid red curves for spin-up electrons and dashed blue curves for spin-down. (b,c) Projected transmission coefficients onto the $NiCp_2$ frontier molecular orbitals as a function of energy for the (b) spin-up and (c) spin-down electrons.

molecule−electrode couplings are rooted in the different electronic structures of the corresponding infinite molecular wires: $[FeCp]_\infty$ is a half-metal, while $[NiCp]_\infty$ is only a spin-degenerate normal metal.

In conclusion, we have investigated the electronic structure and the spin-transport properties of Ni_nCp_{n+1} clusters attached to Au electrodes *via* a variety of anchoring geometries resulting in different electrode−molecule coupling strengths. Although the ground state of the infinite $[NiCp]_\infty$ chain is spin-degenerate, most of the finite Ni_nCp_{n+1} clusters have a spin triplet or doublet ground state and their frontier molecular orbitals are composed of Ni $3d_{xz}$ or $3d_{yz}$ atomic orbitals and π-orbitals of the Cp rings. When attached to Au electrodes through the weak Au−Cp bond (**I**) or the modest face-to-face geometry (**II**), both the $NiCp_2$ and Ni_4Cp_5 clusters do exhibit large spin polarization, reflecting their electronic structure in the gas phase. In contrast, the strong coupling of the clusters with Ni adatoms (**III**) destroys almost completely the spin polarization of all four Ni_nCp_{n+1} clusters investigated but significantly enhances their transmission around the Fermi level. This is realized thanks to the $3d_{xz}$ and $3d_{yz}$ orbitals of the Ni adatoms, which efficiently couple the E_1-like frontier molecular orbitals of the central Ni_nCp_{n+1} cluster to the conducting states of the electrodes. When compared to Fe_nCp_{n+1} ($n > 2$) clusters, which all exhibit both large spin polarization and large transmission around E_F when sandwiched between Pt electrodes through Pt adatoms, the spin-transport properties of Ni_nCp_{n+1} clusters appear to be tunable by the different molecule−electrode coupling. These findings are helpful for the design of future molecular electronic and spintronic devices based on organometallic multidecker clusters.

TABLE 2. Zero-Bias Conductance of the Nickelocene $NiCp_2$ Molecule Contacted to Two Gold Electrodes with Different Molecule−Electrode Anchoring Geometries, Along with the CSP and the SFE

coupling	$G_\uparrow$ [a] (μS)	$G_\downarrow$ (μS)	CSP	SFE (%)
I	2.58	1.20	1.88	53.4
II	35.86	0.62	1.47	98.3
i	22.24	15.40	0.81	30.8
III	74.65	74.34	0.01	0.4

[a] $G_\sigma = e^2/hT_\sigma(E_f)$, where e is the electron charge and h is Planck's constant.

COMPUTATIONAL METHOD

Geometry optimization and electronic structure calculations have been performed by using the SIESTA package.[39] The core electrons are described by improved Troullier−Martins pseudopotentials,[40] and the wave functions for the valence electrons are expanded in terms of a finite range numerical basis set. The pseudopotentials of the C, H, Ni, and Au are generated with the atomic valence configurations s^2p^2, s^1, d^9s^1, and $d^{10}s^1$, respectively. By means of an extensive optimization, a user-defined double-ζ polarized (DZP) basis set is constructed for the C, H, and Ni, and a single-ζ polarized (SZP) basis set is used for Au. The Perdew−Burke−Ernzerhof generalized gradient approximation (GGA) for the exchange and correlation functional is used in all our calculations to account for the electron−electron interactions.[41] Geometry optimization is performed by conjugate gradient relaxation until the forces are smaller than 0.03 eV $Å^{-1}$.

The spin-polarized transport calculations have been performed by using the SMEAGOL package,[20,32,33] which is a practical implementation of the NEGF+DFT approach. Since SMEAGOL uses SIESTA as the DFT platform, we employ the same pseudopotentials, basis set, and GGA functional for both the geometry relaxation and the transport. Periodic boundary conditions are applied in the transverse directions. The unit cell of the extended molecule comprises the Ni_nCp_{n+1} cluster and either four or five Au(111) atomic layers with a lateral (3×3) supercell as part of the electrodes. Furthermore, we use an equivalent cutoff of 150.0 Ry for the real space grid. The charge density is integrated over 80 energy points along the semicircle, 18 energy points along the line in the complex plane, and 12 poles in the Fermi distribution (the electronic temperature is 25 meV). The zero-bias transmission function for the spin-up (majority, $\sigma = \uparrow$) and spin-down (minority, $\sigma = \downarrow$) electrons is calculated from the Landauer formula

$$T_\sigma(E) = Tr[\Gamma_1 G_\sigma \Gamma_2 G_\sigma^+](E)$$

where G_σ is the spin-dependent retarded Green's function of the extended molecule and $\Gamma_{1,2}$ are the broadening functions of the left and right electrodes. It should be noted that the broadening functions, $\Gamma_{1,2}$, are independent of spin since the semi-infinite Au electrodes are not spin-polarized. More details about the numerical implementation can be found in the literature.[32]

Acknowledgment. This project was supported by the National Natural Science Foundation of China (No. 60771002), the Ministry of Education (NCET-07-0014), and the MOST of China (Nos. 2006CB932404 and 2007CB936204). S.S. thanks Science Foundation of Ireland for financial support.

REFERENCES AND NOTES

1. Wolf, S. A.; Awschalom, D. D.; Buhrman, R. A.; Daughton, J. M.; von Molnár, S.; Roukes, M. L.; Chtchelkanova, A. Y.; Treger, D. M. Spintronics: A Spin-Based Electronics Vision for the Future. *Science* **2001**, *294*, 1488–1495.
2. Sanvito, S. Injecting and Controlling Spins in Organic Materials. *J. Mater. Chem.* **2007**, *17*, 4455–4459.
3. Szulczewski, G.; Sanvito, S.; Coey, M. A Spin of Their Own. *Nat. Mater.* **2009**, *8*, 693–695.
4. Bogani, L.; Wernsdorfer, W. Molecular Spintronics Using Single-Molecule Magnets. *Nat. Mater.* **2008**, *7*, 179–186.
5. Baadji, N.; Piacenza, M.; Tugsuz, T.; Della Sala, F.; Maruccio, G.; Sanvito, S. Electrostatic Spin Crossover Effect in Polar Magnetic Molecules. *Nat. Mater.* **2009**, *8*, 813–817.
6. Kandalam, A. K.; Rao, B. K.; Jena, P.; Pandey, R. Geometry and Electronic Structure of $V_n(Bz)_m$ Complexes. *J. Chem. Phys.* **2004**, *120*, 10414–10422.
7. Wang, J.; Acioli, P. H.; Jellinek, J. Structure and Magnetism of V_nBz_{n+1} Sandwich Clusters. *J. Am. Chem. Soc.* **2005**, *127*, 2812–2813.
8. Xiang, H.; Yang, J.; Hou, J. G.; Zhu, Q. One-Dimensional Transition Metal-Benzene Sandwich Polymers: Possible Ideal Conductors for Spin Transport. *J. Am. Chem. Soc.* **2006**, *128*, 2310–2314.
9. Maslyuk, V. V.; Bagrets, A.; Meded, V.; Arnold, A.; Evers, F.; Brandbyge, M.; Bredow, T.; Mertig, I. Organometallic Benzene–Vanadium Wire: A One-Dimensional Half-Metallic Ferromagnet. *Phys. Rev. Lett.* **2006**, *97*, 097201/1–097201/4.
10. Koleini, M.; Paulsson, M.; Brandbyge, M. Efficient Organometallic Spin Filter between Single-Wall Carbon Nanotube or Graphene Electrodes. *Phys. Rev. Lett.* **2007**, *98*, 197202/1–197202/4.
11. Miyajima, K.; Yabushita, S.; Knickelbein, M. B.; Nakajima, A. Stern–Gerlach Experiments of One-Dimensional Metal-Benzene Sandwich Clusters: $M_n(C_6H_6)_m$ (M = Al, Sc, Ti, and V). *J. Am. Chem. Soc.* **2007**, *129*, 8473–8480.
12. Mallajosyula, S. S.; Parida, P.; Pati, S. K. Organometallic Vanadium–Borazine Systems: Efficient One-Dimensional Half-Metallic Spin Filters. *J. Mater. Chem.* **2009**, *19*, 1761–1766.
13. Wang, L.; Cai, Z.; Wang, J.; Lu, J.; Luo, G.; Lai, L.; Zhou, J.; Qin, R.; Gao, Z.; Yu, D.; *et al.* Novel One-Dimensional Organometallic Half Metals: Vanadium–Cyclopentadienyl, Vanadium–Cyclopentadienyl–Benzene, and Vanadium–Anthracene Wires. *Nano Lett.* **2008**, *8*, 3640–3644.
14. Nagao, S.; Kato, A.; Nakajima, A.; Kaya, K. Multiple-Decker Sandwich Poly-Ferrocene Clusters. *J. Am. Chem. Soc.* **2000**, *122*, 4221–4222.
15. Kruse, P.; Johnson, E. R.; DiLabio, G. A.; Wolkow, R. A. Patterning of Vinylferrocene on H-Si(100) *via* Self-Directed Growth of Molecular Lines and STM-Induced Decomposition. *Nano Lett.* **2002**, *2*, 807–810.
16. Zhou, L.; Yang, S. W.; Ng, M. F.; Sullivan, M. B.; Tan, V. B. C.; Shen, L. One-Dimensional Iron–Cyclopentadienyl Sandwich Molecular Wire with Half Metallic, Negative Differential Resistance and High-Spin Filter Efficiency Properties. *J. Am. Chem. Soc.* **2008**, *130*, 4023–4027.
17. Shen, L.; Yang, S. W.; Ng, M. F.; Ligatchev, V.; Zhou, L.; Feng, Y. Charge-Transfer-Based Mechanism for Half-Metallicity and Ferromagnetism in One-Dimensional Organometallic Sandwich Molecular Wires. *J. Am. Chem. Soc.* **2008**, *130*, 13956–13960.
18. Shen, X.; Yi, Z.; Shen, Z.; Zhao, X.; Wu, J.; Hou, S.; Sanvito, S. The Spin Filter Effect of Iron–Cyclopentadienyl Multidecker Clusters: the Role of the Electrode Band Structure and the Coupling Strength. *Nanotechnology* **2009**, *20*, 385401/1–385401/9.
19. Zhang, X.; Wang, J.; Gao, Y.; Zeng, X. *Ab Initio* Study of Structural and Magnetic Properties of $TM_n(ferrocene)_{n+1}$ (TM = Sc, Ti, V, Mn) Sandwich Clusters and Nanowires ($n = \infty$). *ACS Nano* **2009**, *3*, 537–545.
20. Rocha, A. R.; Garcia-Suarez, V. M.; Bailey, S. W.; Lambert, C. J.; Ferrer, J.; Sanvito, S. Towards Molecular Spintronics. *Nat. Mater.* **2005**, *4*, 335–339.
21. Waldron, D.; Haney, P.; Larade, B.; MacDonald, A.; Guo, H. Nonlinear Spin Current and Magnetoresistance of Molecular Tunnel Junctions. *Phys. Rev. Lett.* **2006**, *96*, 166804/1–166804/4.
22. Ning, Z.; Zhu, Y.; Wang, J.; Guo, H. Quantitative Analysis of Nonequilibrium Spin Injection into Molecular Tunnel Junctions. *Phys. Rev. Lett.* **2008**, *100*, 056803/1–056803/4.
23. Meir, Y.; Wingreen, N. S. Landauer Formula for the Current through an Interacting Electron Region. *Phys. Rev. Lett.* **1992**, *68*, 2512–2515.
24. Thygesen, K. S. Electron Transport through an Interacting Region: The Case of a Nonorthogonal Basis Set. *Phys. Rev. B* **2006**, *73*, 035309/1–035309/8.
25. Hohenberg, P.; Kohn, W. Inhomogeneous Electron Gas. *Phys. Rev.* **1964**, *136*, B864–B871.
26. Kohn, W.; Sham, L. J. Self-Consistent Equations Including Exchange and Correlation Effects. *Phys. Rev.* **1965**, *140*, A1133–A1138.
27. Xue, Y.; Datta, S.; Ratner, M. A. First-Principles Based Matrix Green's Function Approach to Molecular Electronic Devices: General Formalism. *Chem. Phys.* **2002**, *281*, 151–170.
28. Ke, S.-H.; Baranger, H. U.; Yang, W. Electron Transport through Molecules: Self-Consistent and Non-Self-Consistent Approaches. *Phys. Rev. B* **2004**, *70*, 085410/1–085410/12.
29. Taylor, J.; Guo, H.; Wang, J. *Ab Initio* Modeling of Quantum Transport Properties of Molecular Electronic Devices. *Phys. Rev. B* **2001**, *63*, 245407/1–245407/13.
30. Brandbyge, M.; Mozos, J.-L.; Ordejón, P.; Taylor, J.; Stokbro, K. Density-Functional Method for Nonequilibrium Electron Transport. *Phys. Rev. B* **2002**, *65*, 165401/1–165401/17.
31. Zhang, J.; Hou, S.; Li, R.; Qian, Z.; Han, R.; Shen, Z.; Zhao, X.; Xue, Z. An Accurate and Efficient Self-Consistent Approach for Calculating Electron Transport through Molecular Electronic Devices: Including the Corrections of Electrodes. *Nanotechnology* **2005**, *16*, 3057–3063.
32. Rocha, A. R.; García-Suárez, V. M.; Bailey, S.; Lambert, C.; Ferrer, J.; Sanvito, S. Spin and Molecular Electronics in Atomically Generated Orbital Landscapes. *Phys. Rev. B* **2006**, *73*, 085414/1–085414/22.
33. Rungger, I.; Sanvito, S. Algorithm for the Construction of Self-Energies for Electronic Transport Calculations Based on Singularity Elimination and Singular Value Decomposition. *Phys. Rev. B* **2008**, *78*, 035407/1–035407/13.
34. Hedberg, L.; Hedberg, K. Molecular Structure of Dicyclopentadienylnickel $(C_5H_5)_2Ni$. *J. Chem. Phys.* **1970**, *53*, 1228–1234.
35. BelBruno, J. J. Half-Sandwich Metal Atom Complexes with Benzene: A Model for Adsorption onto Graphite. *Surf. Sci.* **2005**, *577*, 167–174.
36. Li, R.; Hou, S.; Zhang, J.; Qian, Z.; Shen, Z.; Zhao, X. Analysis on the Contribution of Molecular Orbitals to the Conductance of Molecular Electronic Devices. *J. Chem. Phys.* **2006**, *125*, 194113/1–194113/6.

37. Paulsson, M.; Brandbyge, M. Transmission Eigenchannels from Nonequilibrium Green's Functions. *Phys. Rev. B* **2007**, *76*, 115117/1–115117/7.
38. Hou, S.; Chen, Y.; Shen, X.; Li, R.; Ning, J.; Qian, Z.; Sanvito, S. High Transmission in Ruthenium−Benzene−Ruthenium Molecular Junctions. *Chem. Phys.* **2008**, *354*, 106–111.
39. Soler, J. M.; Artacho, E.; Gale, J. D.; García, A.; Junquera, J.; Ordejón, P.; Sánchez-Portal, D. The SIESTA Method for *Ab Initio* Order-N Materials Simulation. *J. Phys.: Condens. Matter* **2002**, *14*, 2745–2779.
40. Troullier, N.; Martins, J. Efficient Pseudopotentials for Plane-Wave Calculations. *Phys. Rev. B* **1991**, *43*, 1993–2006.
41. Perdew, J.; Burke, K.; Ernzerhof, M. Generalized Gradient Approximation Made Simple. *Phys. Rev. Lett.* **1996**, *77*, 3865–3868.